Supporting information

Buckling-Inspired Multilayer Superhydrophobic Surfaces with Integrated Photo/Electro-Thermal Capabilities for Ultra-Low-Temperature Anti-Icing and De-Icing

Bowen Ji,[‡1] Tianchi Chen,[*‡1,2] Qingxi Li,[1] Minghui Shao,[1] Lianchao Sheng,[1] and Xiangning Lu,[*1].

1. School of Mechanical and Electrical Engineering, Jiangsu Normal University, Xuzhou 221000, China.

2. Sichuan Key Technology Engineering Research Center for All-electric Navigable Aircraft, Sichuan Guanghan, 618307, China)

*Corresponding author：ctc900112@163.com，lxnam89@163.com

‡ These authors contributed equally to this work.

Total number of pages: 24

Total number of figures: 31

Total number of tables: 1

Total number of movies: 2

Contents

1. Synthesis and testing details

1.1 Synthesis of CuS nanoparticles

$CuSO_4$ was used as the copper source, sodium citrate trihydrate was used as the stabilizer, and ascorbic acid (AA) was used as the reducing agent, Cu_2O nanocrystalline cubes were prepared through a one-step nucleation method. First, 0.0441g of sodium citrate trihydrate and 200mL of deionized water were added to a 500 mL round-bottom flask, and the mixture was stirred at room temperature until complete dissolution. Then, 0.5mL of $CuSO_4$ (1.2 M) solution was added and the mixture was stirred for another 5 minutes, resulting in a blue solution. Next, 0.5mL of NaOH (4.8M) solution was added, and the blue color of the solution deepened further. After another 5 minutes of stirring, 0.5mL of ascorbic acid (AA, 1.2M) solution was added and the mixture was stirred at room temperature for 30 minutes. The resulting yellow dispersion was centrifuged at 10000r/min for 10 minutes, then washed three times with deionized water, dried in a 50℃ oven, and the yellow Cu_2O powder was collected. 0.05g of the prepared Cu_2O powder and 20mL of deionized water were added to a 250mL conical flask. After 10 minutes of ultrasonic treatment, 50mL of Na_2S (0.015 M) solution was injected into the solution and the reaction was stirred for 20 minutes. The product was centrifuged at 10000 r/min for 10 minutes, the supernatant was discarded, the product was washed twice with deionized water, and dried at 50℃ to collect the dark green CuS powder.

We conducted the characterization (XRD) of the CuS particles as Fig. 2. The XRD pattern revealed six new characteristic peaks at 27.9, 29.6, 32.1, 48.4, 53.3, and 59.5, corresponding to the (102), (103), (006), (110), (108), and (116) crystal planes of CuS. These peaks are consistent with the CuS standard card (PDF#06-0464), confirming the successful synthesis of CuS.

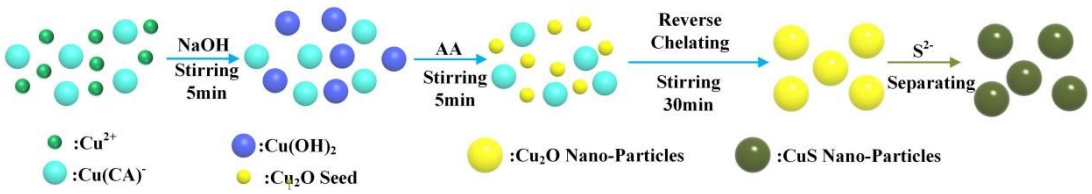

Fig. 1The preparation process of CuS nanoparticles.

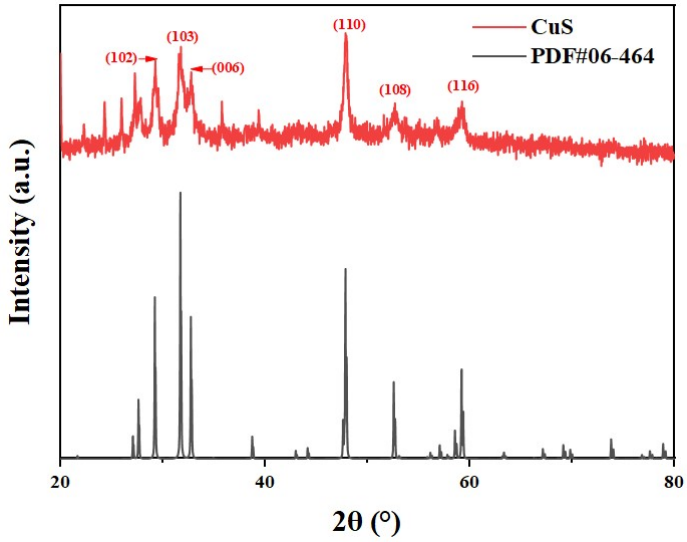

Fig. 2 XRD of the CuS particles

1.2 Mechanical durability and chemical stability tests

The mechanical robustness of the composite superhydrophobic coating was evaluated by sandpaper abrasion tests, impact cycling test and tape peeling test. For the sandpaper abrasion tests, the sample was placed horizontally on the table with the 400# sandpaper in contact with the sample. A 100 g weight (~ 2.2 kPa) is placed on the sample and a horizontal force is applied. It moves at a speed of 5 cm/s. A total of 50 cycles were carried out, and the sliding distance of each cycle was 20cm. After 50 cycles, CA and SA were measured respectively. For the sand impact cycling test, 200 g sand particles with diameters ranging from 100 to 200 mesh were released freely from a sand container placed ~35 cm above the sample which was tilted by 45° in each impact cycle. The WCA and SA were measured after five abrasion cycles. For the tape peeling test, the sample was subjected to 10 consecutive peeling cycles using Scotch tape (3.5 N/cm adhesion force), with a 90° peeling angle at 10 mm/s. After 60 cycles, CA and SA were measured respectively.

Chemical stability was assessed by chemical solution soaking test and measurements of wetting behavior in several chemical solutions. Firstly, WCA and SA of EPS was measured by aqueous solutions with different pH values ranging from 1 to 14. The as-prepared samples were immersed in water, acid solution (pH = 1, hydrochloric acid adjustment) and alkali solution (pH = 10, sodium hydroxide adjustment), and ethanol. After the test time of 24h, the samples were washed

and dried. Then contact and sliding angles were measured subsequently.

1.2 Passive anti-icing, active deicing and ice adhesion experiments

The passive anti-icing and active deicing performance of the coatings were investigated in a environmental test chamber (GDW-0150, Wuxi Nanya Sci-Tech Co., Ltd, China). To evaluate the passive anti-icing performance of the coatings, the freezing process and the icing delay time of the droplets (20 μl) on the uncoated substrates and EPS in the -10 °C - -70 °C, relative humidity = 35 ± 5% environment were recorded with a camera. The icing delay time was defined as the time for a droplet to change from liquid phase to solid phase until it was completely transformed into ice during the freezing process. Tin (icing nucleation time) is defined as the time it takes the droplet to contact the surface from transparent to opaque, and Tif (icing freezing time) is the transition from the beginning of the phase transition to a fully frozen droplet.

In order to evaluate the active deicing performance of the coatings, a camera was used to record the time when the ice melted completely away from the coating surface under the simulated solar radiation (1sun) of the xenon light source and different power density (0.1-0.3w/cm^2) under the environment of -40℃ to -70℃. The active deicing process and the deicing time were recorded with a camera.

The samples were placed in a environmental test chamber with the temperature and humidity set to -30°C and 35 ± 5% RH, respectively. A acrylic column with a base area of 100 mm^2 and a height of 5cm was placed on the samples, deionized water was injected into the column, and the deionized water was completely frozen after 1 hours. After the samples were completely fixed, the force transducer was mounted on the motion stage to push the column at a rate of 0.2mm/s. The maximum force was recorded to calculate the ice adhesion strength by the equation:

$$\tau_{ice} = \frac{F_{max}}{A} \quad \text{(S1)}$$

where A stands for the contact area between the ice and surface. ice adhesion strength were average values for 3 times.

2. Calculation and Modeling details

S1. Calculating the light absorption efficiency

Light absorbance of the samples is calculated through the following equation:

$$A\%= 1-R\%-T\% \quad (S3)$$

where A is the absorbance, R is the reflectance, and T is the transmittance.

S2. Calculating the photo-thermal conversion efficiency

The photo-thermal conversion efficiency of samples, η, which was defined as the ratio of the heat generated by the photo-thermal conversion of the surface to the input of solar power, and the calculation formula is as follows:

$$\eta = \frac{Q}{q \times A} \quad (S4)$$

where Q is the total heat generated by the surface, q represents the light intensity of sunlight (1kW/m2), A is the surface area of the surface (6.25 cm^2).

When the surface temperature of samples and the surrounding temperature gradually reach a balance, the heat generated by the surface can be calculated as follows:

$$Q = h \times A \times (T_{sub} - T_{surr}) \quad (S5)$$

where h is the convective heat transfer coefficient of the substrate, A is the heat transfer area, Tsub is the equilibrium temperature of the surface, and Tsurr is the temperature of surrounding temperature.

The convective heat transfer coefficient of the samples can be calculated by the following equation:

$$h = \frac{N\mathrm{u} \times \lambda}{L} \quad (S6)$$

where L is the characteristic length of heat transfer area (L=2.5), λ is the thermal conductivity of air, Nu is the Nusselt number, and can be calculated as follows:

$$N\mathrm{u} = 0.54 \times (Gr \times \mathrm{Pr})_m^{1/4} \quad (S7)$$

where $Gr = \frac{g a_v \Delta T L^3}{v^2}$ is the Grashof number, Pr is the prandtl number, the m represents qualitative temperature, which use arithmetic average temperature of the boundary layer ($T_m = \frac{T_{sub} + T_{surr}}{2}$). a_v is the expansion coefficient of air ($a_v = \frac{1}{T}$), T is the average of the sum of the initial ambient and equilibrium temperatures of the sample, g is the gravitational acceleration (9.8 m/s^2). Δ T is the value of the temperature difference in surface from room temperature to equilibrium temperature, v is the viscosity coefficient.

S3 DFT Calculation

The calculations for the Lowest Unoccupied Molecular Orbital (LUMO), Highest Occupied Molecular Orbital (HOMO), and Electrostatic Potential (ESP) were performed using the Gaussian16

program package. Molecular optimization was carried out with Density Functional Theory (DFT) at the B3LYP/6-31G (d, p) level, in conjunction with DFT-D3(BJ) dispersion correction. The electrostatic potential (ESP) of the van der Waals surface projection was obtained using Multiwfn 3.8 (dev)[1]. Isosurface maps were generated with the VMD visualization program, based on files exported by Multiwfn. Independent gradient model based on Hirshfeld partition (IGMH) was used to analyze weak interactions between molecular bonds via Multiwfn[2]. Standard coloring of the sign (λ2) ρ in the IGMH diagram were ranging from blue, green to red, meaning strong attraction (hydrogen bond, halogen bond, etc), Van der Waals' force, and strong repulsion, respectively. The binding energy (ΔE) of the optimized molecules was calculated at the B3LYP-D3(BJ)/def2-TZVP level. ΔE was defined as the difference between the complex and the sum of energies of monomers.

S4 Simulation of droplet impact on elastic surfaces

The finite element simulation was performed by COMSOL to analysis the droplet impacting behavior on elastic surfaces. The flow-solid coupling calculation can be performed using the phase field and solid mechanics modules. Before simulation, the following conditions were set:

(1)A 2-D model is adopted. The droplet has an initial velocity of zero and falls under the action of gravity. The evaporation and sublimation of water were neglected.

(2) The wettability wall was set to 154.1° on the superhydrophobic surface. The movement of air and water was set to laminar flow model. The diameter of water droplet is about 1.7 mm and the drop height of the liquid is 20 mm,which is consistent with the experiment data.

(3) For the material, we invoked the strong assumption of linear elastic material. As such, the following values for material properties were used: density ρ= 970 kg/m^3, Young's modulus E=750 kPa, and Poisson's ratio ν= 0.3. The networks of the whole model was set to hyperfine structure. The minimum interval step of time simulation was 0.5 ms.

S5. The heat-transfer model of a droplet on the uncoated hydrophilic surface, superhydrophobic surface and EPS with flexible supporting layer under cold conditions.

The finite element simulation methods were performed by COMSOL, and the detailed method was explained as follows:

The initial ambient temperature was -20 °C, the initial temperature of water droplet was 0 °C. We neglected the evaporation of water and sublimation of ice in the cooling conditions.

The CA of the water droplet on the superhydrophobic surface was 150°.

The classical heat and mass transfer equations were still feasible.

$$\frac{\partial(\rho C_p T)}{\partial t} + \nabla(\rho C_p u T) = \nabla[\nabla(kT)] \tag{S8}$$

The networks near the heat transfer interfaces was set to hyperfine structure. The minimum interval step of time simulation was 0.001s.

S6. The Light absorption and heat-transfer model of EPS

To obtain the electric field in the system, our COMSOL model solves the time-independent electromagnetic wave equation[3].

$$\nabla \times \nabla \times E(r,\omega) - k_0^2 \varepsilon(r,\omega) E(r,\omega) = 0 \qquad \text{(S9)}$$

where E is the electric field, k_0 is the free space wavenumber, $\varepsilon(r,\omega)$ is the space- and wavelength-dependent relative permittivity of the material, and ω is the angular frequency of the incident light. The conversion of optical energy to thermal energy can be described by Equation (S10)[4]

$$\rho C_p \frac{\partial T}{\partial t} - \nabla \cdot (k \nabla T) = Q_r - Q_c \qquad \text{(S10)}$$

where T is the temperature, t is the time, and ρ, C_p, and k are the density, specific heat capacity, and thermal conductivity of the considered material, respectively; furthermore, Q_r is the local heat power of the CuS absorber. The generated heat power Q_r can be obtained from Equation (S11)[5]

$$Q_r = \frac{\omega \varepsilon_0}{2} Im\{\varepsilon(r,\omega)\} |E(r,\omega)|^2 \qquad \text{(S11)}$$

where ε_0 is the vacuum permittivity and $Im\{\varepsilon(r,\omega)\}$ is the imaginary part of the permittivity. Q_c is the dissipated energy transferred from the absorber to the external environment, which can be expressed as

$$Q_c = B(T - T_{amb}) \qquad \text{(S12)}$$

where B is the thermal transfer coefficient from the absorber to the external environment, and T_{amb} is the environment temperature (293.15 K)

3.Supplementary Figures

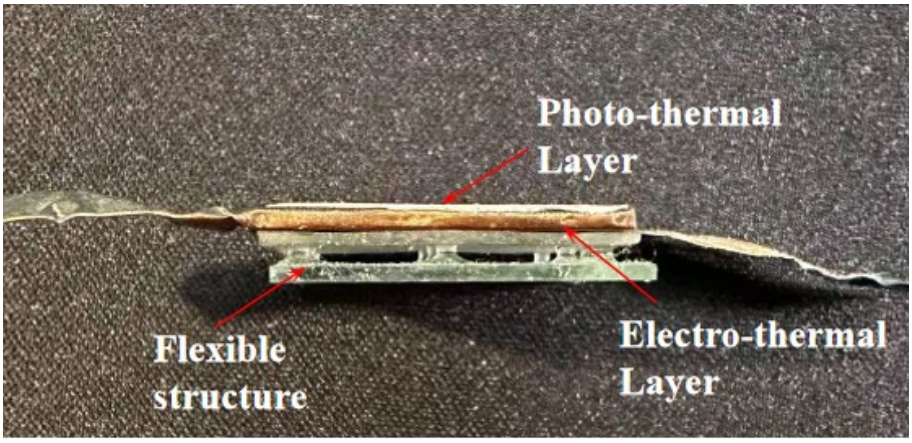

Fig. S1 Optical image of EPS

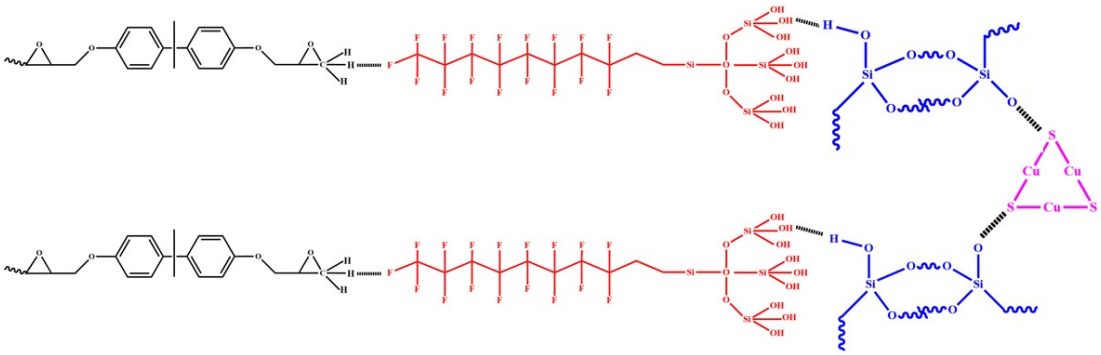

Fig. S2 Schematic illustration of the formation mechanism of the EPS.

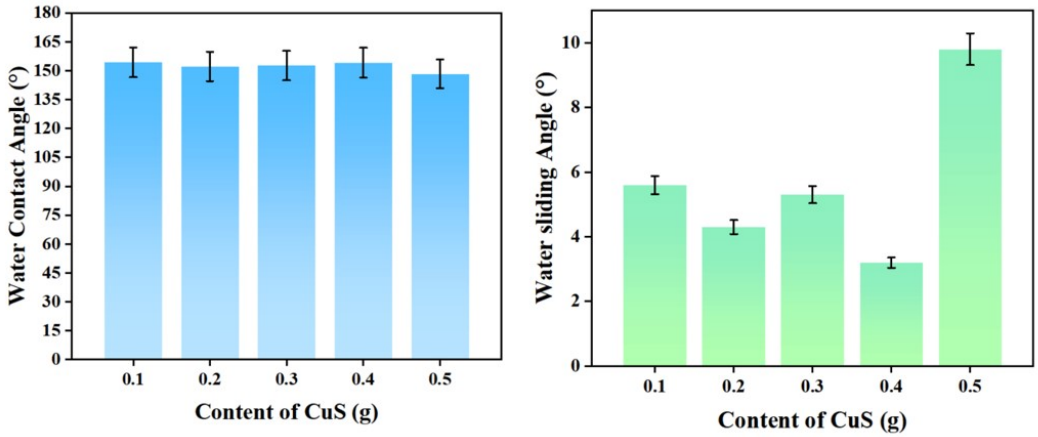

Fig. S3 EPS water contact angles and sliding angles with different contents of CuS

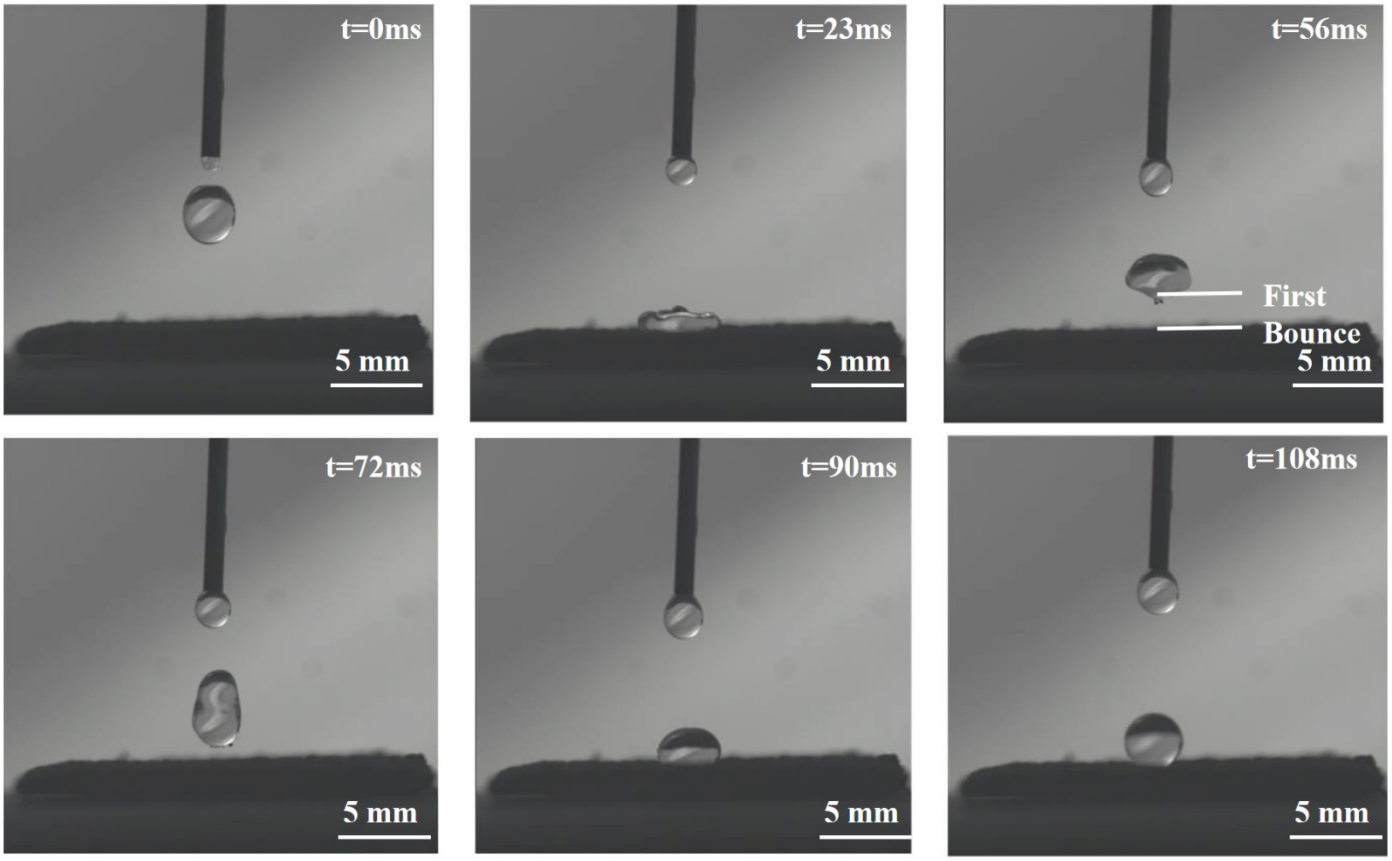

Fig. S4 Photos of the bouncing process of 20 μL water droplets falling from 20 mm above the surface of the superhydrophobic coating.

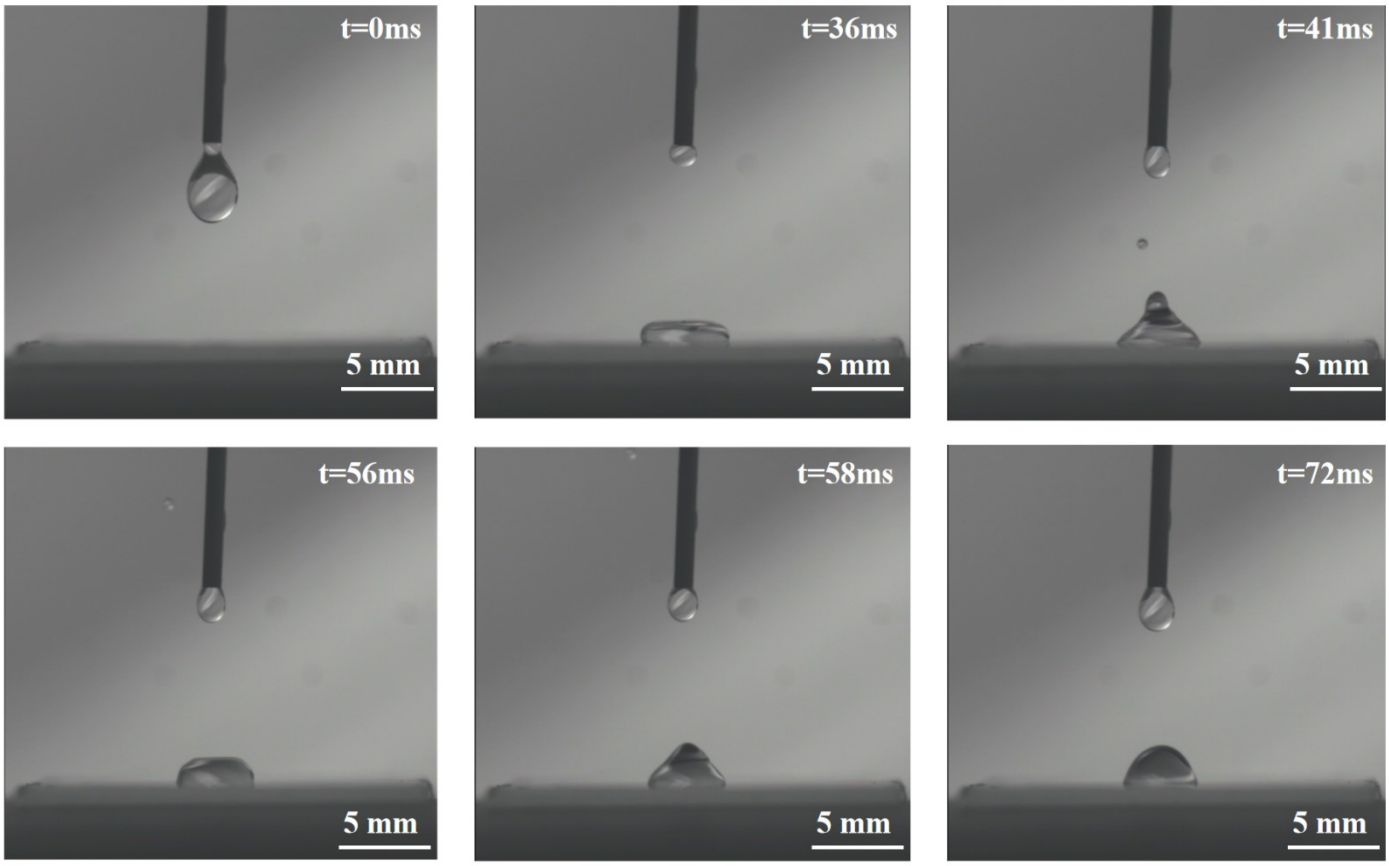

Fig. S5 Photos of the bouncing process of a 20 μL water droplet when it falls 20 mm above the surface of a glass substrate.

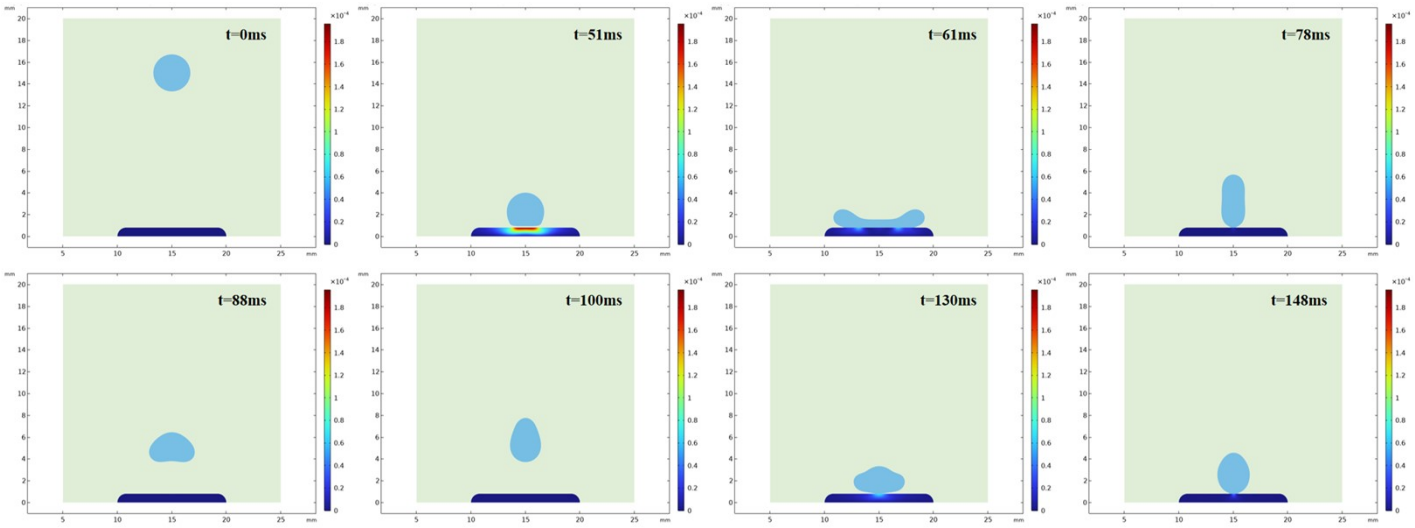

Fig.S6 Simulation results of water droplet rebound on a rigid surface.

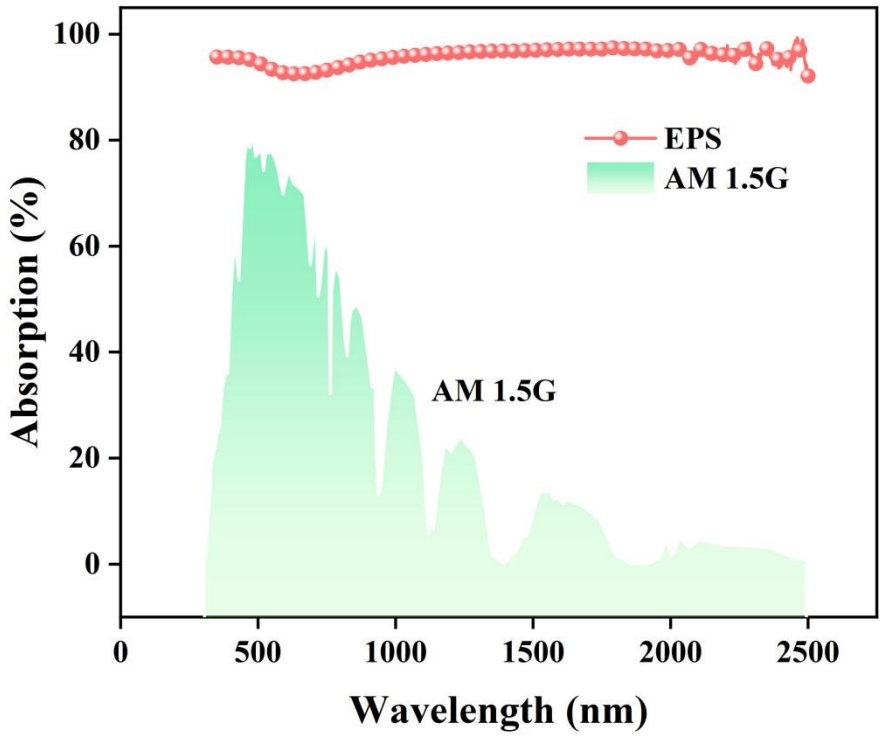

Fig. S7 The light absorption spectrum in the 250-2000 nm wavelength range of the EPS

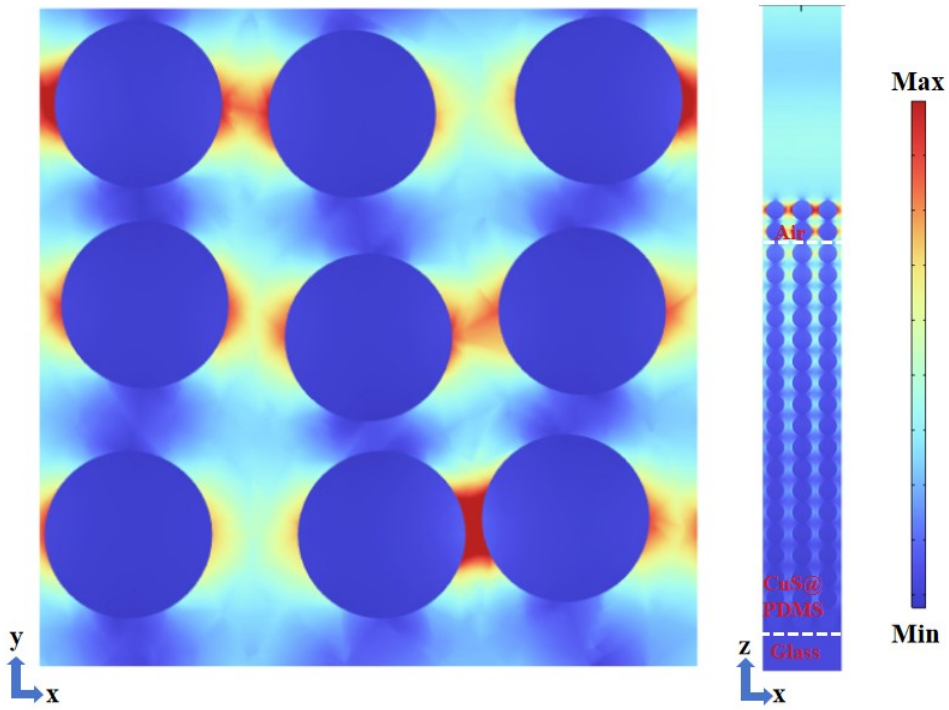

Fig. S8 Electrical field distributions in the x–y and x–z planes for the CuS absorber (808 nm as incident light).

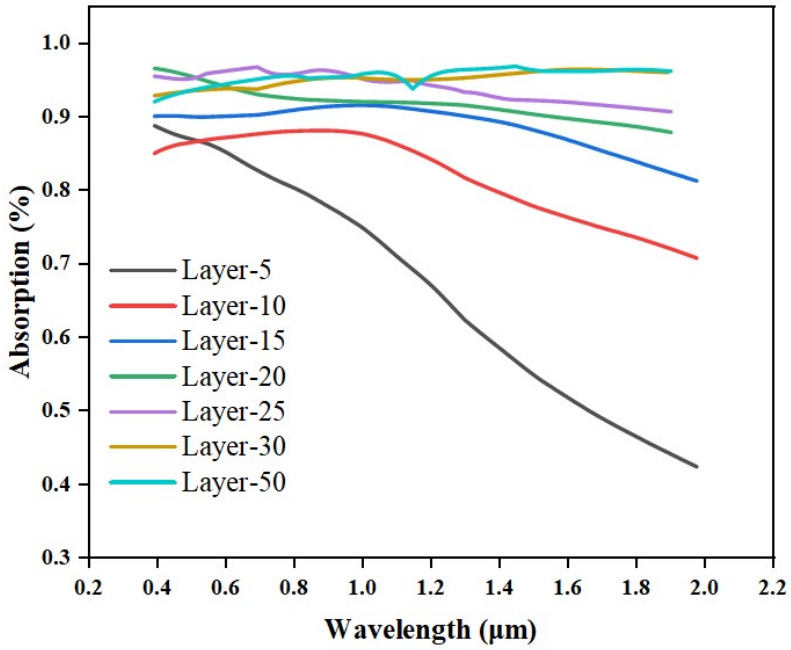

Fig. S9 The light absorption rate curves of different layers of CuS

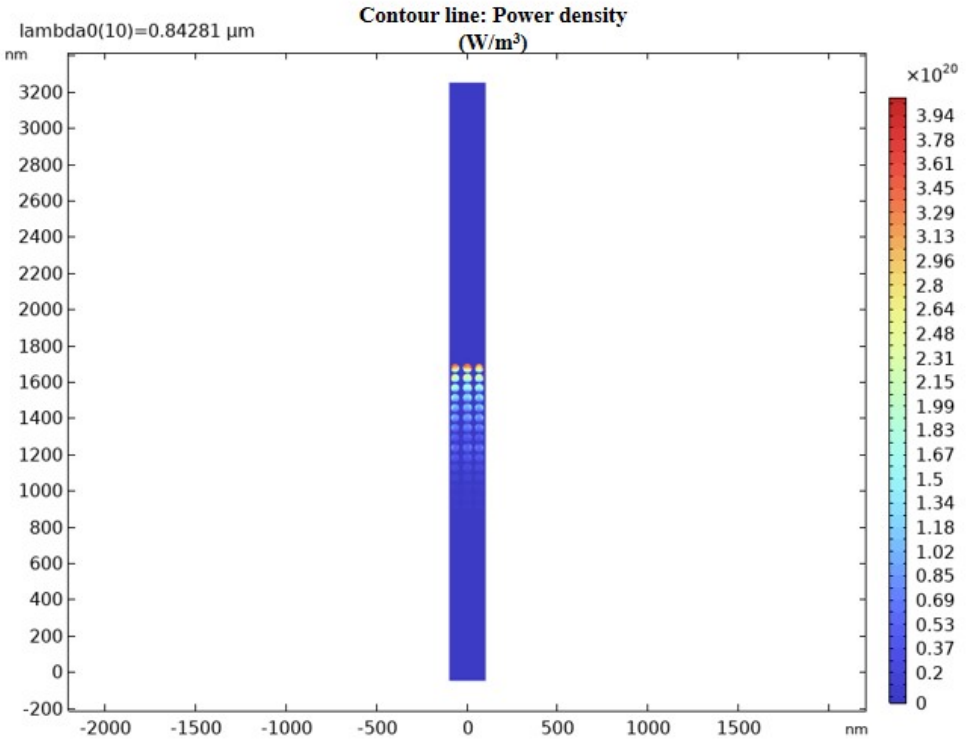

Fig. S10 The total power density of the CuS layer-30

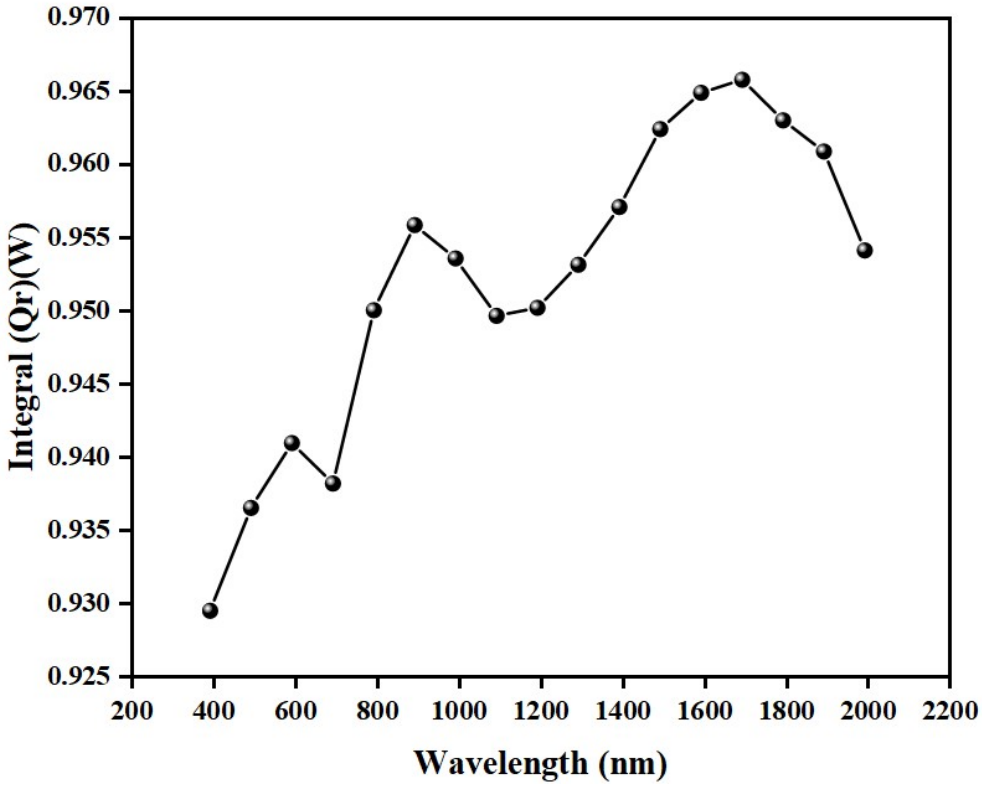

Fig. S11The integral (Qr) of the CuS layer-30

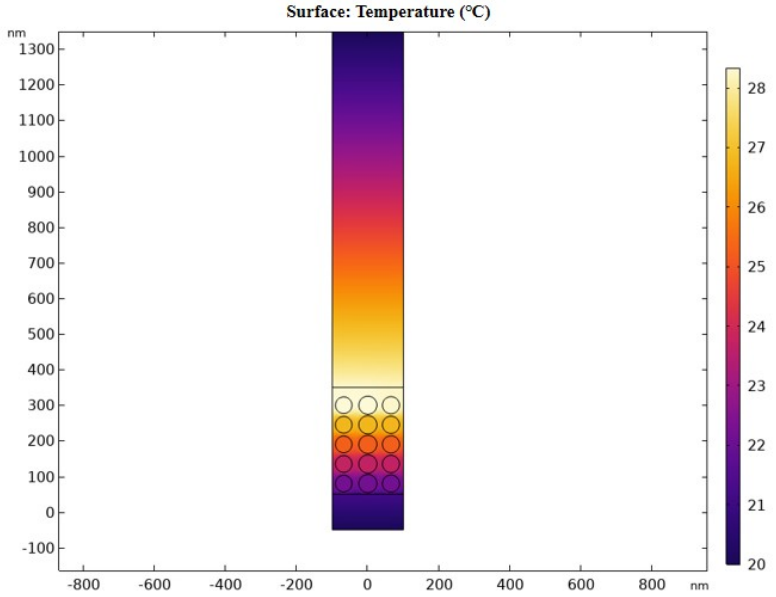

Fig. S12 Simulation results of surface temperature of the CuS layer-5

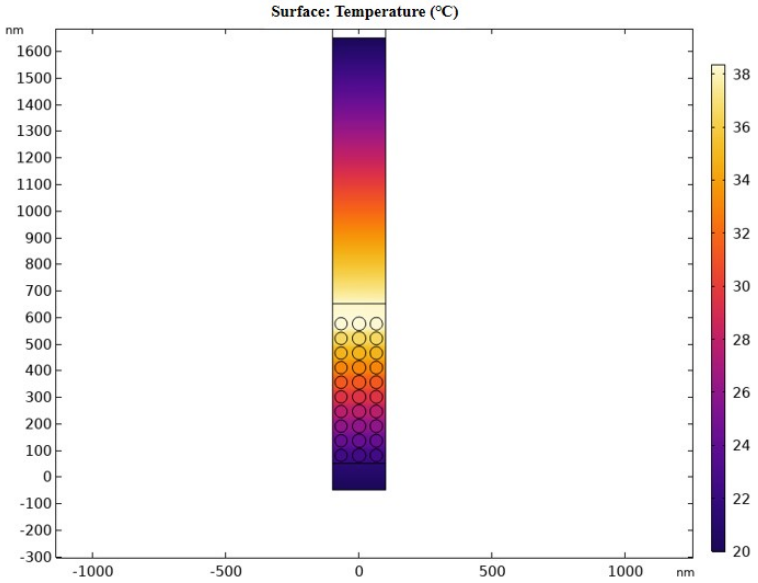

Fig. S13 Simulation results of surface temperature of the CuS layer-10

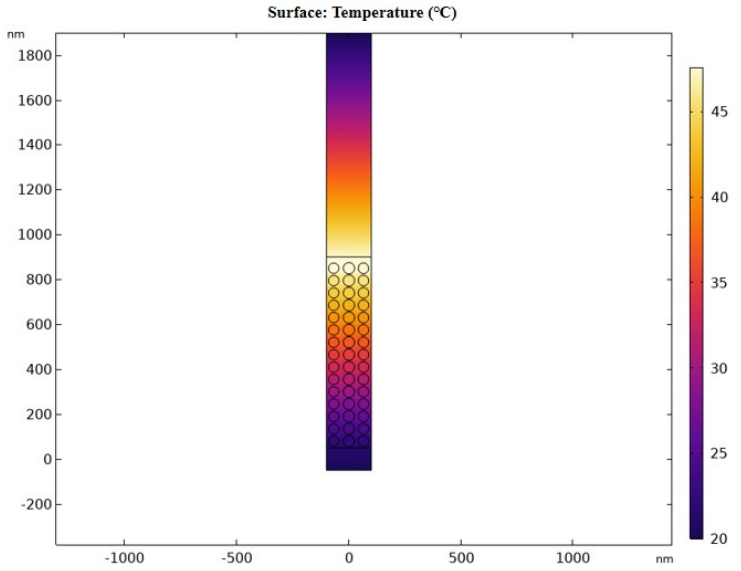

Fig. S14 Simulation results of surface temperature of the CuS layer-15

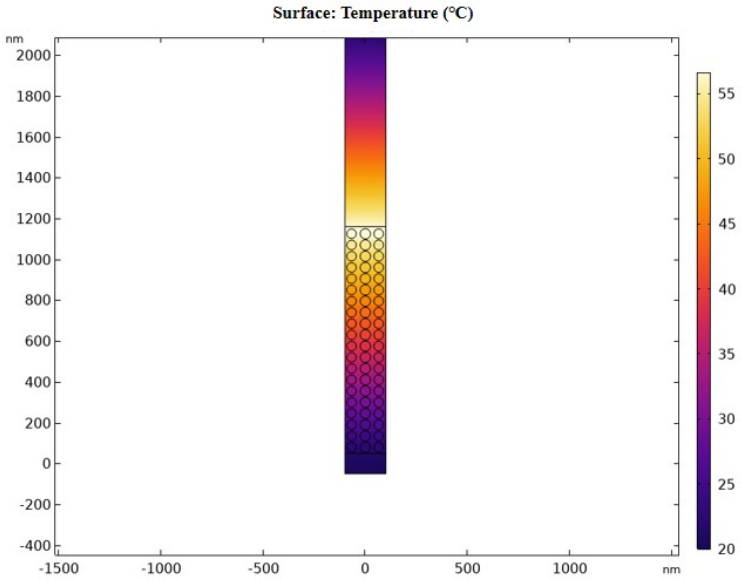

Fig. S15 Simulation results of surface temperature of the CuS layer-20

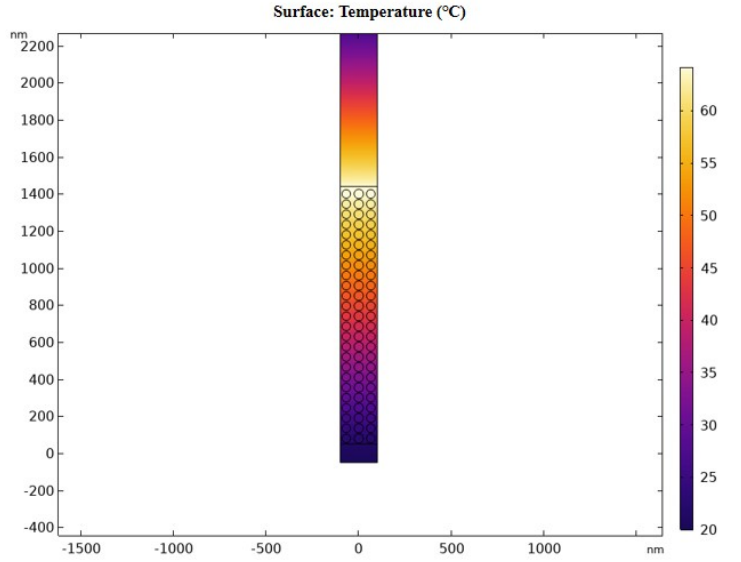

Fig. S16 Simulation results of surface temperature of the CuS layer-25

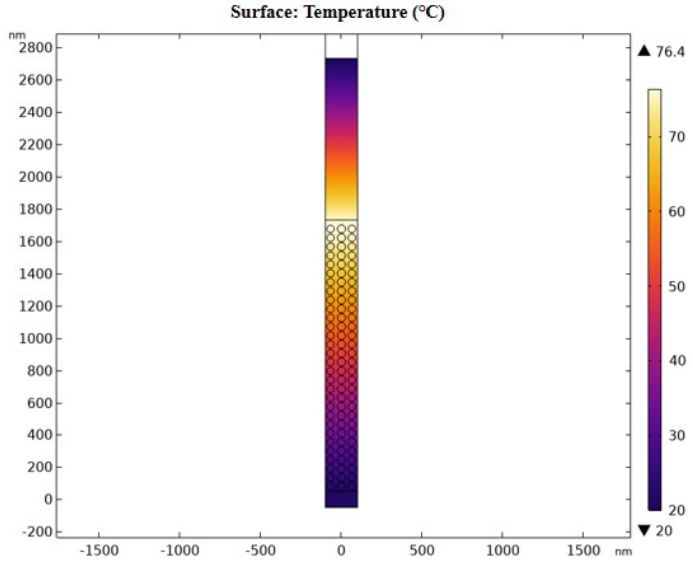

Fig. S17 Simulation results of surface temperature of the CuS layer-30

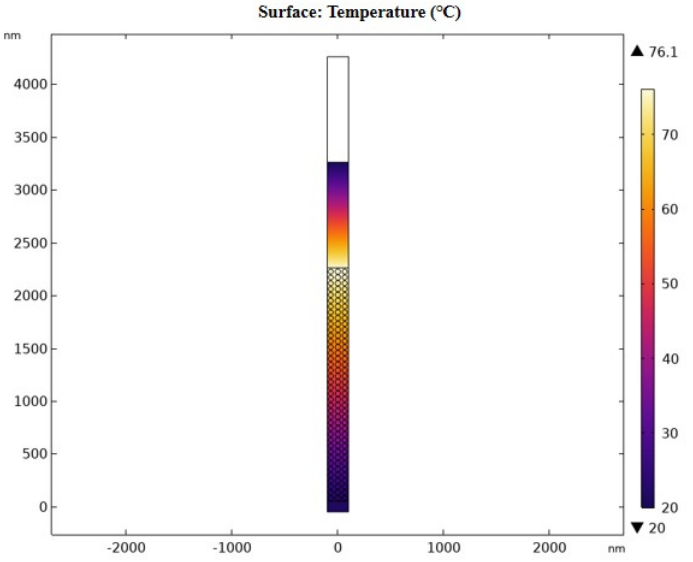

Fig. S18 Simulation results of surface temperature of the CuS layer-50

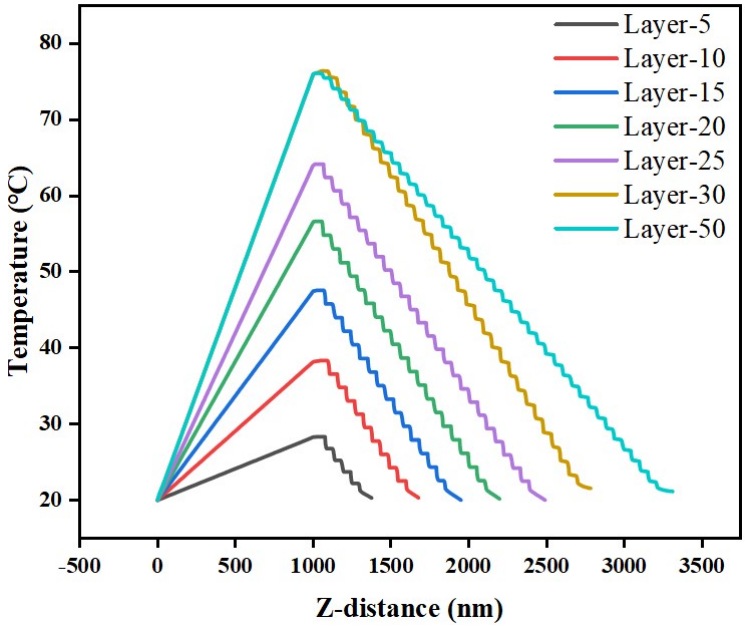

Fig. S19 The relationship between temperature distribution and z position for different numbers of CuS layers

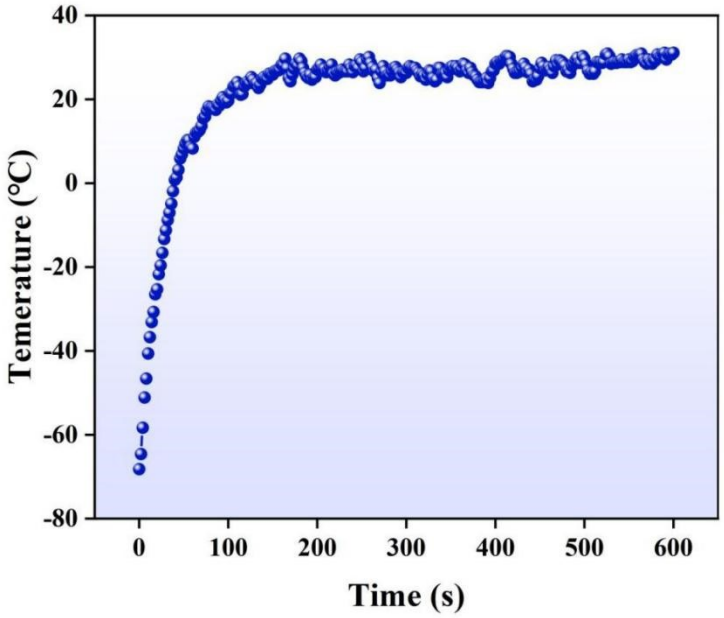

Fig. S20 The temperature-time curve of EPS at -70°C under a current density of 0.3w/cm^2

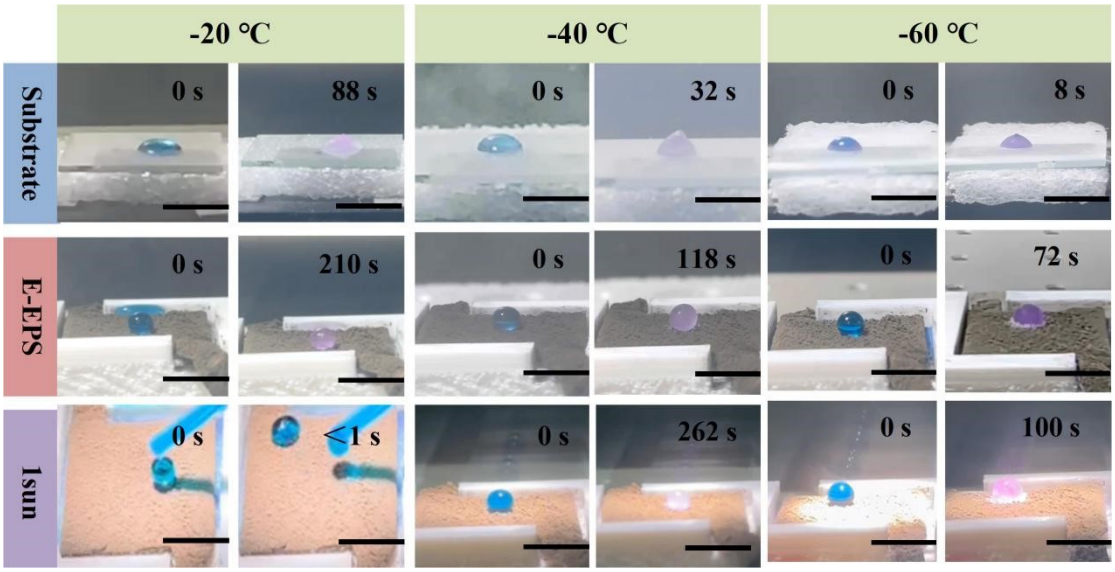

Fig. S21 Icing delay processes of untreated surfaces, EPS, and 1 Sun EPS at -20 ℃, -40 ℃, and -60 ℃

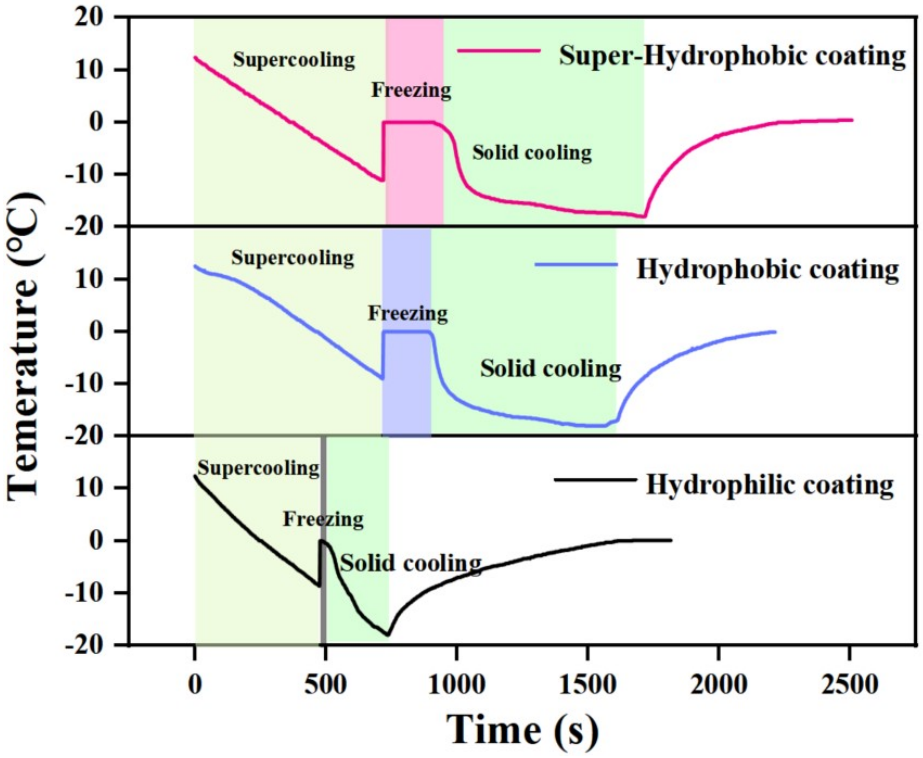

Fig. S22 The freezing process of water droplets on hydrophilic, hydrophobic and superhydrophobic surfaces at -20℃

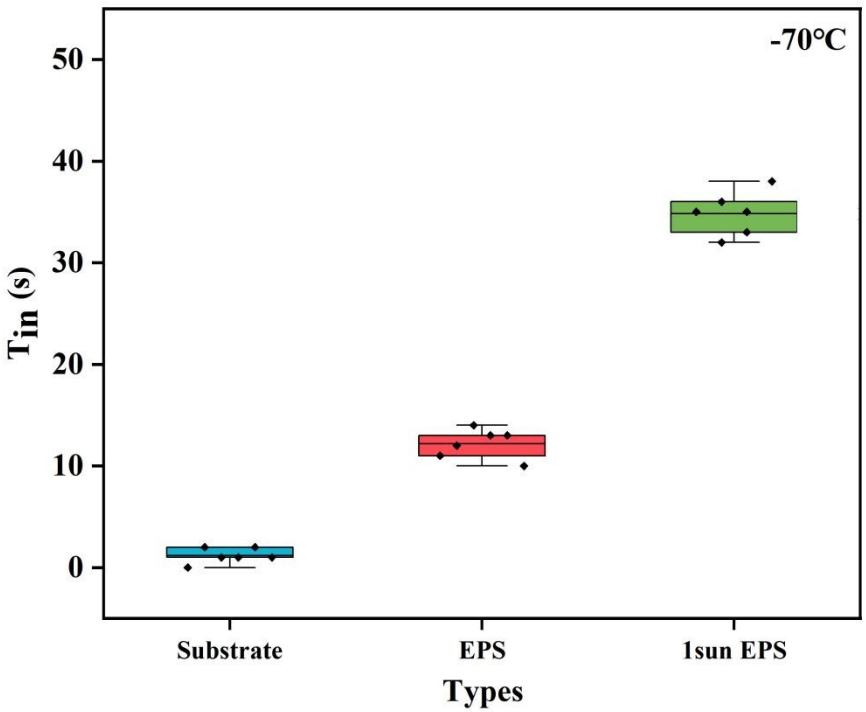

Fig. S23 The stability of T_{in} in EPS during the icing delay process at -70℃.

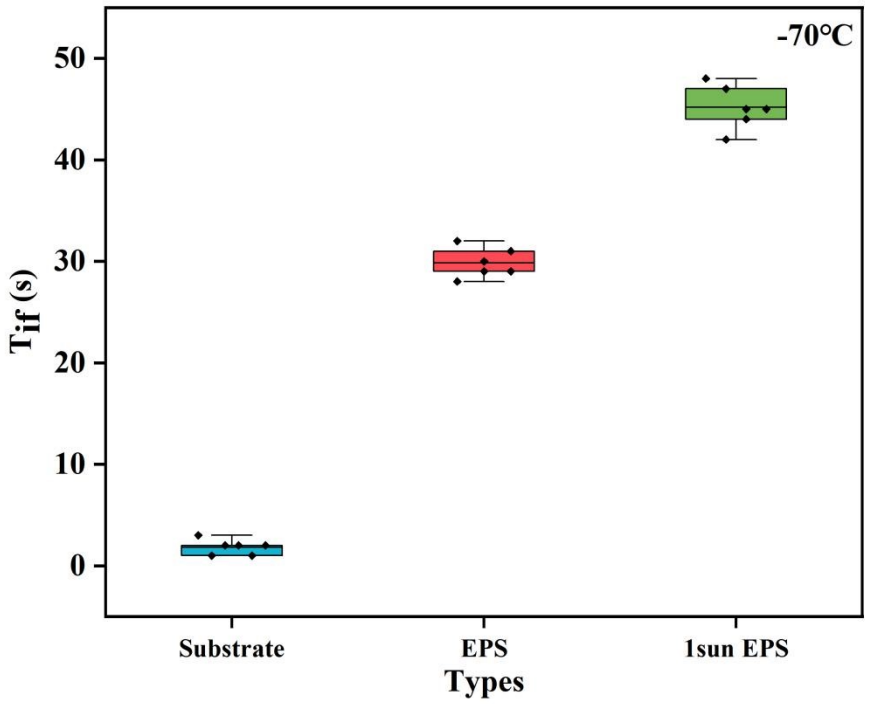

Fig. S24 The stability of T_{if} in EPS during the icing delay process at -70℃

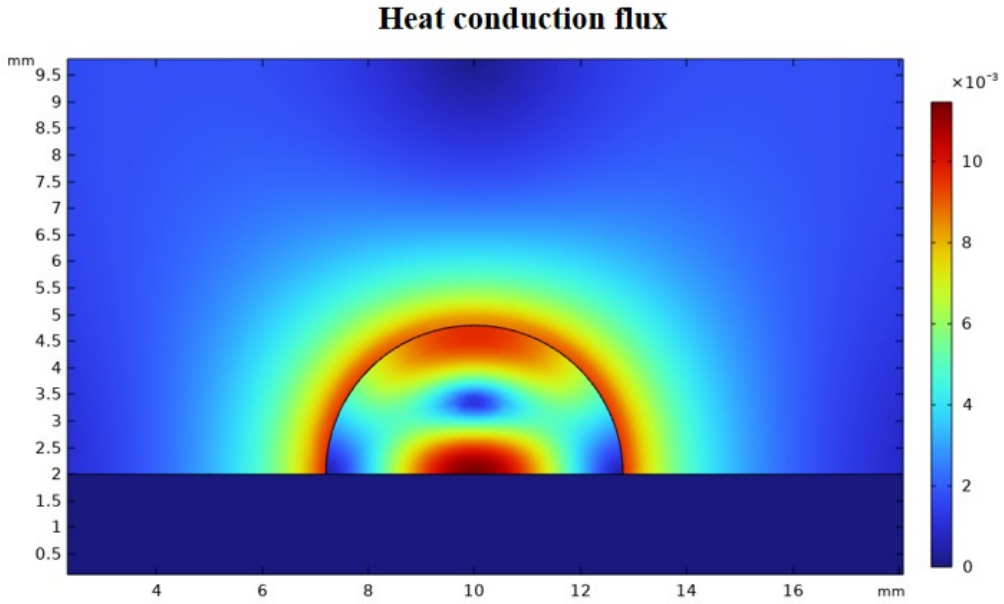

Fig. S25 The Heat conductive flux of hydrophilic surface irradiationat -20 ℃

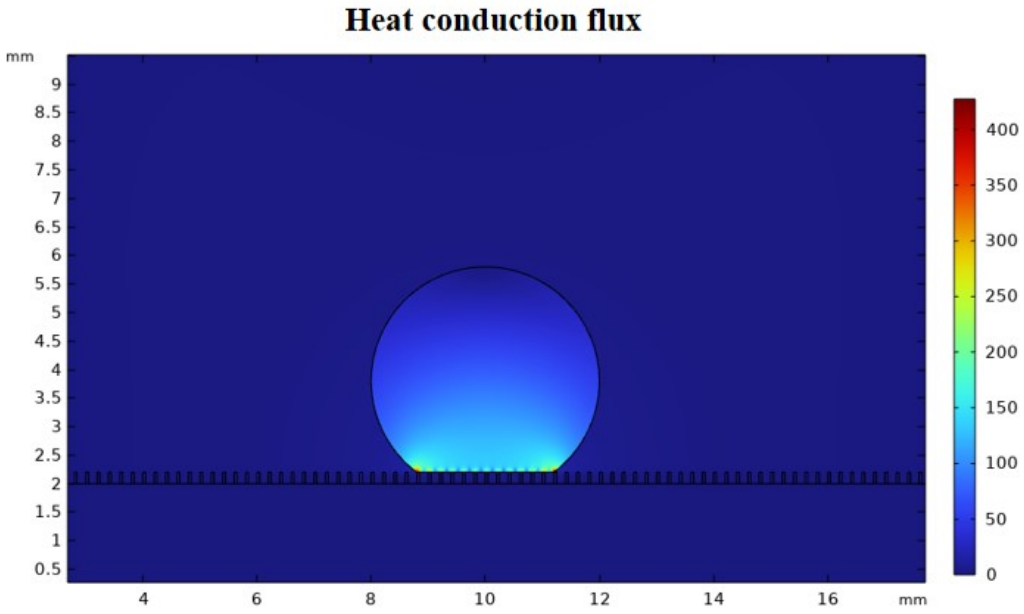

Fig. S26 The Heat conductive flux of superhydrophobic surface irradiation at -20 ℃

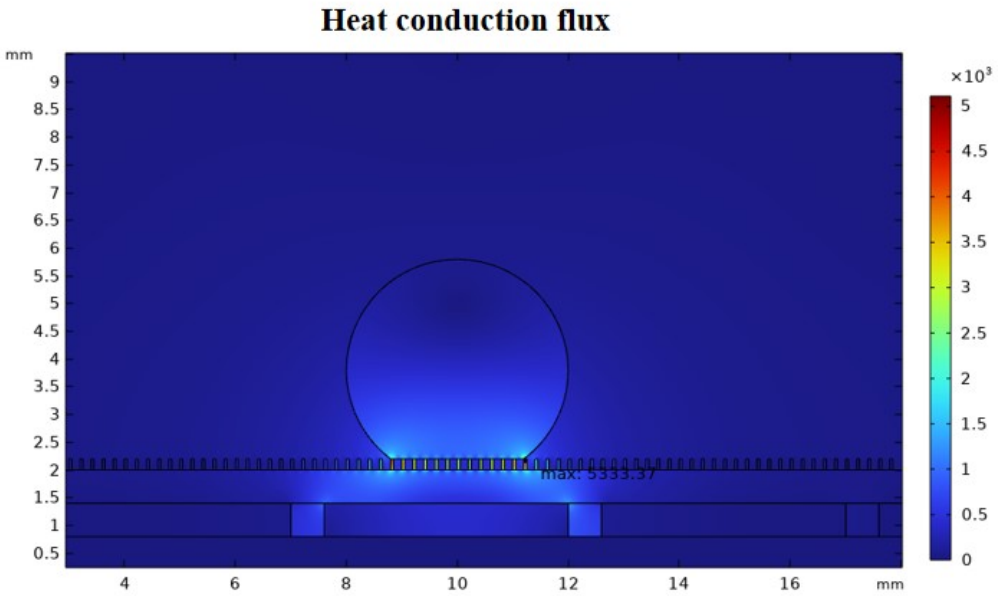

Fig. S27 The Heat conductive flux of EPS irradiation at -20 ℃

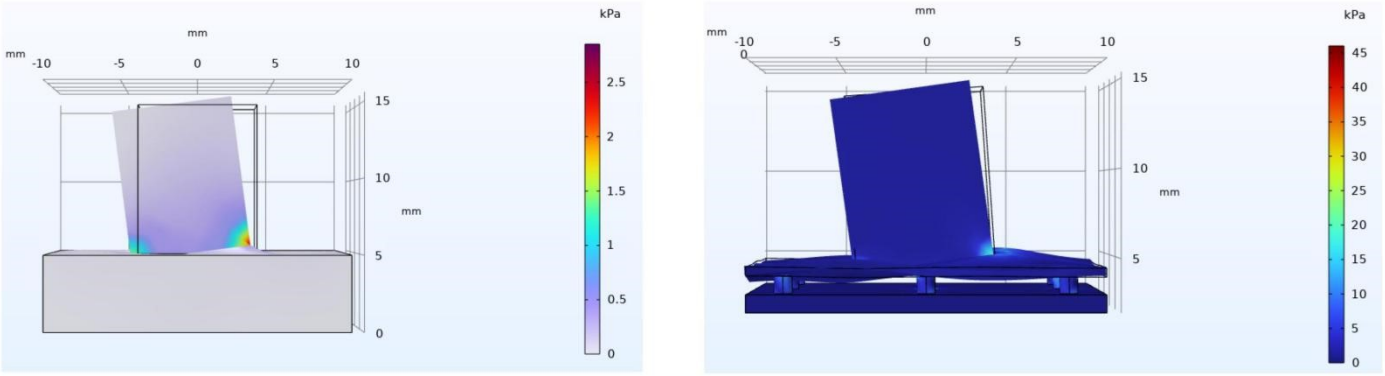

Fig. S28 The stress of the unstructured substrate and EPS (3x3)

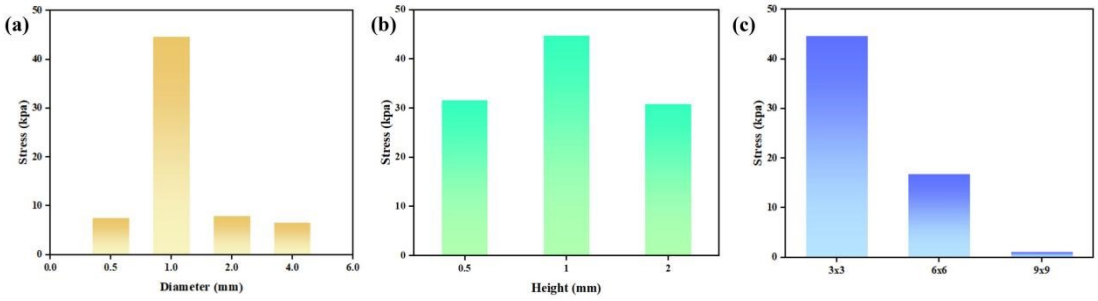

Fig. S29 The simulation results of stress on micro-columns of different heights and diameters

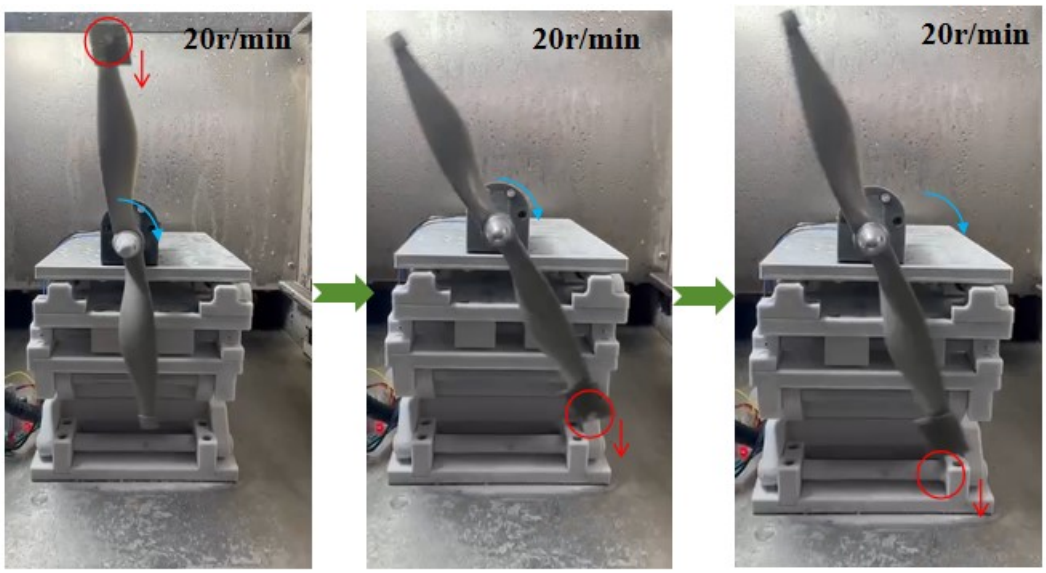

Fig. S30 Experiment of simulated wind turbine on SH surface at -20℃.

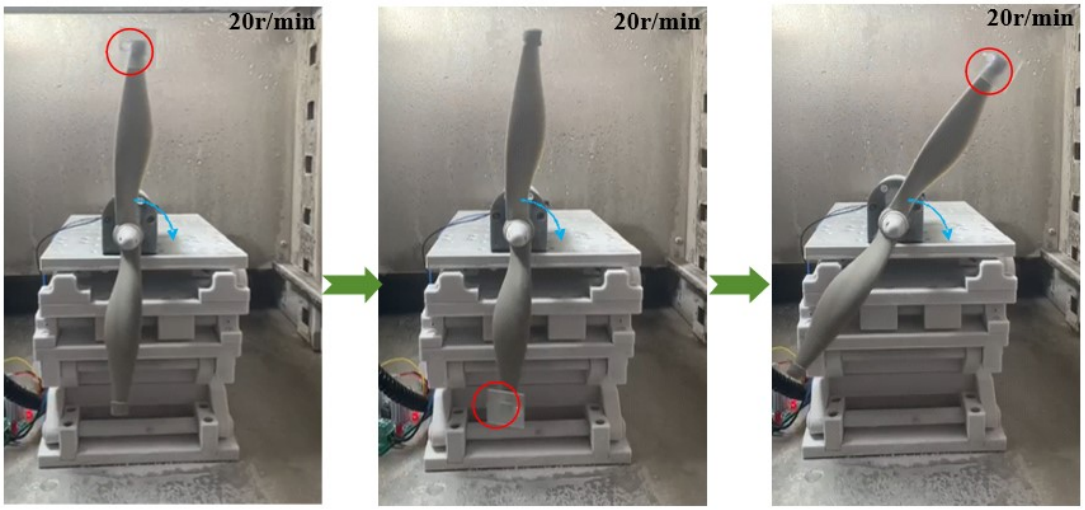

Fig. S31 Experiment of simulated wind turbine on substrate at -20℃

4. Supplementary Table

Active Photo/Eletro-thermal deicing		Anti-icing/deicing performances			Ref.
Photo-thermal	**Electro-thermal**	**Rate of delayed freezing time[%]**	**Ice adhesion strength[kPa]**	**Temperature[℃]**	
64 ℃ (1 sun)	55 ℃ (0.2 w/cm^2)	540%		28.2℃(-**30℃**±1℃，RH：85%±5%)	[6]
69.3 ℃ (1 sun)	205 ℃ (1w/cm^2)	600%		10.8℃(-**10℃**±1℃，RH：60%±5%)	[7]
39℃ (1 sun)	95℃ (25V,)	1150%	105.2(-20℃)	11℃(**-15℃**)	[8]
18.6℃ (1.2 sun，-30 ℃)	40℃ (15V, -30℃)	1400%		70℃(**-30℃**，RH：26%)	[9]
60℃ (2 sun，-15 ℃)	80℃ (0.3w/cm^2, -20℃)	367%	283(-25℃)	30℃(**-10℃**)	[10]
70.3℃ (1 sun)	62℃ (0.2w/cm^2)	318%		39.2℃(-**20℃**CRH：50%±5%)	[11]
70℃ (1 sun)	120℃ (12V)	10000% (1 sun)	80(-30℃)	**-15℃**	[12]
71.9℃ (1 sun)		284%	45.85(-20℃)	-**20℃**,RH:35±5%	[13]
80.2℃ (1 sun)		8000%	46.75(-20℃)	5.3℃(-**35℃**,RH:35±5%)	[14]
63.7℃ (1 sun)	94.7℃ (2V)	1711%		34℃ (**-20℃**)	[15]
88.6℃ (1 sun)	122℃ (20V)	1615%	40(-15℃)	90℃ (**-15℃**)	[16]
	62.5℃ (0.15w/cm^2, -30℃).		80(-20℃)	62.5℃ (-**30℃,** RH:60%)	[17]
	78℃ (0.35w/cm^2, -43℃).			-35℃	[18]
30℃(1 sun)		113%		15℃(-15℃)	[19]
32℃(1 sun)				26.7℃(-15℃)	[20]
82.8℃ (1 sun)	224.6 ℃ (0.3w/cm^2)	1400% (-70℃)	4.38kPa(-30℃)	30.4℃(**-70℃,** RH:35±5%)	**This work**

	Never freezing (-30℃)

5. Supplementary Movies

Movie S1: Photo/Eletro-thermal deicing process at different temperatures (ranging from -40 ℃ to -70 ℃)
Movie S2: Photo/Eletro-thermal deicing process at different temperatures (ranging from -40 ℃ to -70 ℃)

6. Supporting References

1 T. Lu, Q. Chen, *J. comput. Chem.* **2022**, 43(8): 539-555.

2 T. Lu, *J. Chem. Phys*. **2024**, 161 (8).

3 C. Hong, S. Yang, J. C. Ndukaife. *Opt. Mater. Express.* **2019,** 9(3): 953-964.

4 C. Ma, P. Yu, W. Wang, Y. Zhu, L. Feng, J. Wang, Z. Jing, X. T. Kong, P. Li, A. Govorov, D. Liu, H. Xu, Z. Wang, *ACS nano.* **2021**, 15(10): 16357-16367.

5 B. Wang, W. Wang, E. Ashalley, X. Zhang, P. Yu, H. Xu, Z. M. Wang. *J. Phys. D: Appl. Phys*. **2020**, 54, 094001.

6 J. Liu, C. He, B. Liu, Z. Wang, S. Zhao, Z. Lu, Y. Zhang, Z. Tang, X. Gao, X. Aday, *Chem. Eng. J*. **2024**, 489, 151338.

7 L. Wang, K. Yin, Q. Deng, Q. Huang, C. J. Arnusch, *Carbon*. **2024**, 219, 118824.

8 Y. Guo, H. Zhao, C. Zhang, G. Zhao, *Chem. Eng. J*. **2024**, 497, 154383.

9 Y. Liu, R. Xu, N. Luo, Y. Liu, Y. Wu, B. Yu, S. Liu, F. Zhou, *Adv. Mater. Technol*. **2021**, 6, 2100371.

10 Z. Zhao, Y. Wang, Z. Wang, X. Cui, G. Liu, Y. Zhang, Y. Zhu, J. Chen, S. Sun, K. Zhang, X. Liu, H. Chen, *Small* **2024**, 20, 2311435.

11 Q. Chen, X. Shen, Z. Zhang, Q. Xu, *Prog. Org. Coat*. **2024**, 191, 108438.

12 Y. Cheng, Y. Wang, X. Zhang, J. Zhang, Z. He, J. Wang, J. Zhang, *Nano Res*. **2023**, 16, 7171.

13 M. Zheng, C. Zhou, Q. Liu, X. Li, Y. Yang, Y. Sun, Z. Zhu, Y. Huang, Q.Zhou, *Soft Matter*, **2023**, 19(46): 9036-9049

14 B. Ji, T. Chen, X. Song, L. Sheng, X. Lu, D. Yang. *Soft Matter*, **2024**, 20(40): 8144-8157.

15 J. Huang, Z. Peng, B. Zhang, Y. Yao, S. Chen. *ACS Appl. Mater. Interfaces*, **2024**, 16(33): 44210-44224.

16 L. Liu, S. Chen, Y. Hu, W. Pan, T. Dong, Y. Chen, L. Lin, L. Wang, *Adv. Funct. Mater*, **2024**, 34(40): 2404760.

17 Y. Wan, Y. Liu, Y. Liu, C. Sun, K. Feng, Y. Wu, F. Zhou, *ACS Appl. Eng. Mater*, **2023**, 1(1): 669-678.

18 Z. Zhao, H. Chen, X. Lin, Z. Wang, Y. Zhu, Y. Zhou, *Surf. Coat. Technol*, **2020**, 404: 126489.

19 Y. Ren, M. Hou, Z. Jiang, W. Sun. F. Chu, N. Lai, *Surf. Coat. Technol*, **2024**, 485: 130888.

20 M. Hou, Z. Jiang, W. Sun, Z. Chen, F. Chu, N. Lai, *Adv. Mater*, **2024**, 36(3): 2310312.